AIP | Review of Scientific Instruments

X-ray imaging of subsurface dynamics in high-Z materials at the Diamond Light Source

D. E. Eakins and D. J. Chapman

Citation: Review of Scientific Instruments **85**, 123708 (2014); doi: 10.1063/1.4904275
View online: http://dx.doi.org/10.1063/1.4904275
View Table of Contents: http://scitation.aip.org/content/aip/journal/rsi/85/12?ver=pdfcov
Published by the AIP Publishing

X-ray imaging of subsurface dynamics in high-Z materials at the Diamond Light Source

D. E. Eakins[a] and D. J. Chapman
Institute of Shock Physics, Imperial College London, London SW7 2BZ, United Kingdom

(Received 14 August 2014; accepted 15 November 2014; published online 22 December 2014)

In this paper, we describe a new approach enabling study of subsurface dynamics in high-Z materials using the unique combination of high-energy synchrotron X-rays, a hybrid bunch structure, and a new dynamic loading platform. We detail the design and operation of the purpose-built, portable small bore gas-gun, which was installed on the I12 high-energy beamline at the Diamond Light Source and used to drive compression waves into solid and porous metal targets. Using a hybrid bunch structure and broadband X-ray pulses of up to 300 keV, radiographic snapshots were captured during various dynamic deformation processes in cm-scale specimens, thereby contributing to a more complete understanding of the evolution of mesoscale damage. Importantly, we highlight strategies for overcoming the challenges associated with using high-energy X-rays, and suggest areas for improvement needed to advance dynamic imaging through large-scale samples of relevance to engineering scenarios. These preliminary measurements demonstrate the feasibility of probing highly transient phenomena using the presented methodology. [http://dx.doi.org/10.1063/1.4904275]

I. INTRODUCTION

The dynamic mechanical behaviour of materials is an important area of study, having profound relevance to numerous industries involving high-rate processes such as advanced manufacturing, automotive, aeronautics, space, or defence technologies. The high operational stresses and velocities implicit in these applications often lead to sudden and catastrophic failure, which is challenging and expensive to both diagnose and remedy. Developing improved materials for these high-rate environments requires knowledge of their specific failure mechanisms, which may include a wide range of mesoscale phenomena such as void nucleation and coalescence, adiabatic shear localisation, deformation twinning, and/or structural phase transitions.

Our current state of knowledge regarding these underlying processes has largely evolved from a combination of *in situ* time-resolved measurements and post-failure materials characterisation. Traditional time-resolved measurements, such as high-speed photography and optical velocimetry, are in general indirect techniques, insofar as the measurements are removed from the subsurface phenomena of interest. Consequently, much of the details of local deformation and mesoscopic processes, integral to the development and refinement of modern multiscale models, are left unresolved.

The challenge of diagnosing in-material behaviour has historically been met through the use of X-rays,[1] although more recently both proton[2] and neutron imaging and spectroscopy[3–5] have provided insights into in-material phenomena. The range of X-ray sources applied to dynamic materials research has been diverse, from laser-driven backlighters,[6] small conventional capacitor-driven X-ray tubes, large accelerator-driven X-ray machines such as DAHRT,[7] and X-ray free electron lasers.[8] Each of these sources produce specific X-ray characteristics which are suitable to probe different material scales, and hence phenomena.

Recent years have seen growing interest in the use of synchrotron X-rays as a new source for dynamic, materials research. Synchrotrons offer the attractive combination of high brilliance, short pulse durations, and high-energy X-rays suitable for good spatial and temporal resolution imaging. Pioneering work at the Advanced Photon Source has demonstrated the feasibility of performing dynamic phase contrast imaging during impact generated events.[9–11] Using a dedicated small-bore gas-gun on the 32ID beamline, single snapshots of various dynamically loaded targets were captured using 9–12 keV X-rays. The imaging system employed provided an approximately 1.6 mm square field-of-view, with up to 3 μm spatial resolution, sufficient to study a range of dynamic deformation phenomena, including microscale long-rod penetration into B_4C and vitreous carbon plates, comminution of carbon fibres, and brittle fracture in a bed of glass spheres.

In this paper, we introduce a complimentary technique which enables probing of large volumes of material during dynamic compression, with the objective of accessing microstructure information under well-defined loading conditions. We detail the successful synchronisation of a portable gas-gun with a hybrid bunch mode at the Diamond Light Source (DLS), and present some of the first measurements of dynamic deformation and compression processes in materials on the mm-cm scale using high-energy synchrotron X-rays. Specific challenges posed by the high energy of the X-rays, and our on-going efforts to overcome these are discussed.

II. EXPERIMENTAL CONSIDERATIONS

The present work aims to utilise the advantages offered by 3rd generation light sources to reveal subsurface physical processes during the intermediate stages of dynamic

[a]d.eakins@imperial.ac.uk

loading. One of the drivers behind the development of subsurface imaging is in the exploration of damage processes and transformations free from the effect of material surfaces, and thus under a well-defined state. Such a capability allows for extended study of various failure processes, but necessarily involves large, mm-scale targets to avoid premature release, which unavoidably introduces a number of specific challenges:

1. Larger samples require high-energy X-rays for sufficient transmission.
2. The multi-user nature of a national synchrotron facility requires a dynamic loading technique which is portable, and quick to set up.
3. Time-resolved imaging necessitates a method of gating high-energy X-rays or scintillator emission.

The first challenge is caused by the comparatively larger samples required for intermediate timescale studies, as a result of the need to support a well-defined, nominally 1-dimensional shocked state for up to several microseconds. This can only be accomplished by extending the dimensions of the sample to avoid either longitudinal or lateral release overtake from contaminating the stress conditions within the target. For example, one process of interest is the nucleation, growth, and coalescence of voids leading to full spall scab formation. While the nucleation and growth of individual voids is suggested to take place on the picosecond to nanosecond timescale,[12,13] their growth and coalescence into mesoscopic void clusters is a strong function of the underlying defected microstructure, which evolves over the microsecond timescale as a result of the loading history (see, for example, Ref. 14). Another example is the process of rotational dynamic recrystallisation (RDR), which has been proposed as one of the mechanisms responsible for adiabatic shear localisation.[15] This specific microstructural process occurs over several microseconds (at least 6 μs in Ti-6Al-4V) further necessitating the study of large-scale samples.[15,16] These examples serve to demonstrate that in order to study intermediate timescale phenomena we must typically employ samples several mm thick, and hence several tens of mm radially. Correspondingly, X-ray penetration suffers, requiring the use of higher energy X-rays to achieve sufficient transmission.

The second challenge is in generating and diagnosing reliable dynamic loading in a sample and synchronising this compression platform to a synchrotron. This challenge originates from the fact that both synchrotrons and loading platforms are designed to operate independently, neither able to generate an output (either X-rays or a loading state) on demand. In recent examples, loading has been generated using either a small-bore gas-gun or Hopkinson pressure bar.[9–11,17] Such systems are commonly driven with high-pressure gas, in which "firing" is performed through the rapid delivery of this pressure to the back of a projectile or striker bar. This is often accomplished using a high-speed valve, however variations in projectile or o-ring dimensions, barrel cleanliness, system vacuum, and the simple response of the valve itself, result in impact jitter (variation in impact time) on the order of milliseconds. Although advanced triggering schemes exist which reduce this time substantially,[18] timing to within the duration of a single X-ray pulse (tens of ps) has yet to be achieved, and is unlikely to be realised practically. In addition to challenges associated with the timing of the loading platform relative to the synchrotron, the installation of a loading platform such as a gas-gun and the associated diagnostics within an experimental hutch at a synchrotron poses several further logistical challenges, the most significant of which is the physical space requirements for gas-gun systems, typically many meters in length. Additional challenges include the safe integration of traditional shock physics laser based diagnostics within the experimental hutch, and the need to safely operate the gas-gun remotely. These logistical challenges constrain the suitable synchrotron facilities at which the investigation of dynamic phenomena using a gas-gun can be conducted.

The third challenge results from the need for highly penetrating X-rays, and involves the appropriate methods to record information arising from the transmission and scattering of X-rays through the target over short periods of time. This can be accomplished in several ways, however the simplest revolve around either gating the incoming X-rays to limit the exposure of the target, or gating the recording devices to ensure information capture over only the time interval of interest. Gating of the X-rays can be a viable technique, involving the use of a pair of mechanical shutters or choppers, and requires only that subsequent bunches be appropriately spaced to match the reliable activation time of the mechanical shutter system. While this method is feasible for small beam diameters at the microsecond timescale,[19] full attenuation of a large beam (>mm), requires a pair of fast and slow shutters, which can only respond on the ms timescale.[9,20] An alternative method, that of gating the recording devices, can be achieved by operating the software shutter on the recording camera, effectively controlling the voltage to the photocathode and intensifier such that only the scintillator emission bracketing the timescale of interest is amplified by the capture system. The disadvantages of this approach is the constant bombarding of the sample with the X-ray beam, which can lead to undesirable heating of the sample and diagnostics.

III. METHODOLOGY

Dynamic X-ray imaging experiments were performed at the DLS, a 3rd generation synchrotron located at the Harwell Science and Innovation Campus, Didcot, Oxfordshire, UK. The overall approach of the present work is presented in Figure 1(a). A sample is subjected to dynamic loading through direct impact using a gas-gun installed at the end of a synchrotron beamline. During the compression event, high-energy X-rays are scattered through the sample and partially converted into visible light at a crystal scintillator, which in turn is collected by a fast lens and imaged onto an intensified CCD camera. This approach is described in more detail in Secs. III A–III E, with particular emphasis on the X-ray beamline, bunch structure, loading platform, and diagnostic implementation.

A. High-energy beamline

In order to achieve sufficient X-ray transmission through large and/or high-Z samples, experiments were performed

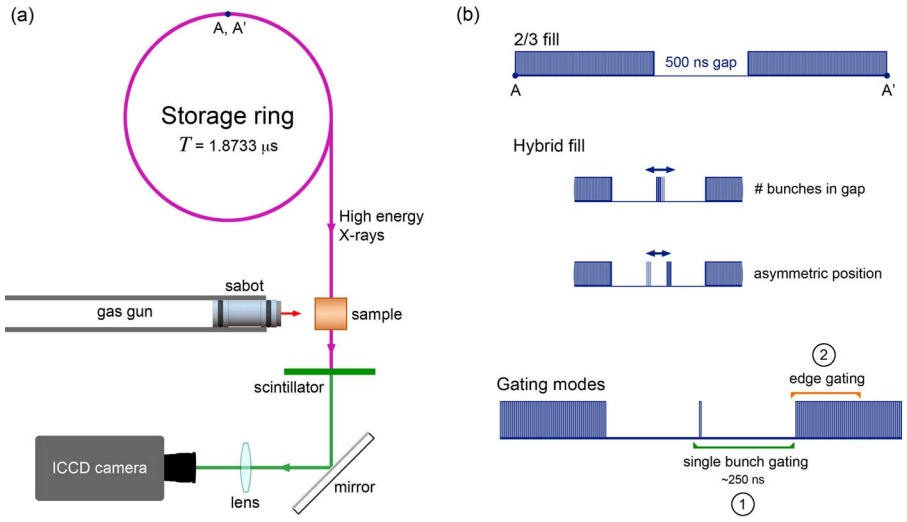

FIG. 1. (a) A simplified overview of the dynamic X-ray imaging experiments. Synchrotron X-rays arrive at the sample, which in turn is dynamically compressed through a high velocity impact process. The transmitted X-rays are absorbed by a scintillator, whose visible emission is recorded by an intensified CCD camera. (b) Illustration depicting the 2/3 and hybrid fill modes of the electron storage ring. The 500 ns gap of the 2/3 fill can be populated, yielding the hybrid fill mode used in these experiments. Also shown are the two gating modes explored in this work; (1) "single bunch" gating brackets from just prior to the single bunch to just before the end of the 500 ns gap (~250 ns), maximising collection of the scintillator emission; (2) "Edge" gating refers to a variable gate width, starting at the beginning of the next period of 2 ns periodic bunches.

on the I12 Joint Engineering, Environmental and Processing (JEEP) beamline. The I12 beam source is a 4.2 T superconducting multi-pole wiggler which can deliver high-energy X-rays in the 20–300 keV range. The beamline has two in-line experimental hutches; the first experimental hutch (EH1) is located in the main experimental hall approximately 50 m from the insertion device. The second experimental hutch (EH2) is located in an external building approximately 95 m from the source, and importantly offers adequate space (11 m long × 7 m wide) to install a dynamic loading platform and associated diagnostics. The I12 beamline can provide a large white or monochromatic beam in EH2 (up to 95 mm horizontally × 30 mm vertically). In the current work, the white beam configuration with a potential flux in EH2 of 5.5 × 10^9 photons s^{-1} mm^{-2} 0.1% bw^{-1} at 150 keV (calculated using XOP[21]) was adopted to maximise the photon flux. However, to avoid unwanted heating of the sample, the X-ray beam was hardened by the addition of a 4 mm Cu filter reducing the on sample flux to 2.5 × 10^9 photons s^{-1} mm^{-2} 0.1% bw^{-1} at 150 keV. At this energy we expect 50% transmission through 4.5 mm of Fe, and similarly through 18 mm of Al (Figure 2), and importantly for the filtered flux a nominal heat load on the sample of 7 mW cm^{-2}, insufficient to cause significant heating of the specimen during the testing process here. These specimen dimensions permit study of 1-dimensional, uniaxial strain conditions over durations ranging from 0.35 μs to 1.25 μs, respectively, allowing access to phenomena which occur at these extended time-scales, and over spatial regimes which closely approach bulk material response.

B. X-ray bunch structure

The standard mode of the 561.6 m, 3 GeV electron storage ring at the DLS is a continuous fill of the 936 total RF buckets. With the RF system running at approximately 500 MHz, this gives ~2 ns spacing between sequential buckets, and a total orbit time of 1.8733 μs.[22] Some flexibility is afforded on the overall bunch structure, provided the storage ring current does not deviate too significantly from 300 mA. DLS can also operate in a "2/3" fill mode, in which 636 consecutive buckets are populated with electrons, and the remaining left empty; this corresponds to a ~500 ns gap of unpopulated buckets (see Figure 1(b)). A single bunch mode is also available, however is typically used during non-user beamtime.

In the present work, a custom fill mode was utilised comprising a combination of the 2/3 fill and single bunch modes. Such modes, wherein individual or multiple RF buckets are populated within the space of the 500 ns gap, are referred to as "hybrid" fills. The current hybrid fill consisted of a single bunch centred within the 500 ns gap, with approximately 3 times the individual bunch current (Figure 1(b)). This was

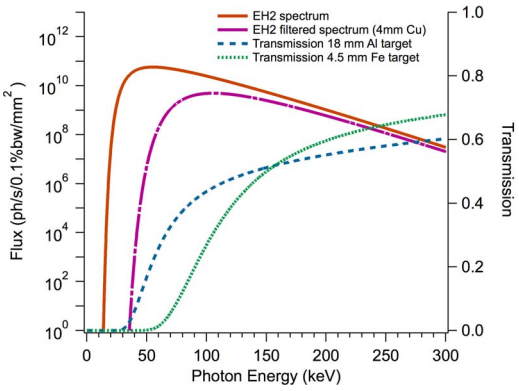

FIG. 2. X-ray spectrum showing the photon flux in EH2 after the fixed filters, and following insertion of an additional 4 mm Cu filter, as used in this work. Also shown are the transmission spectrum for 4.5 mm of Fe and 18 mm of Al.

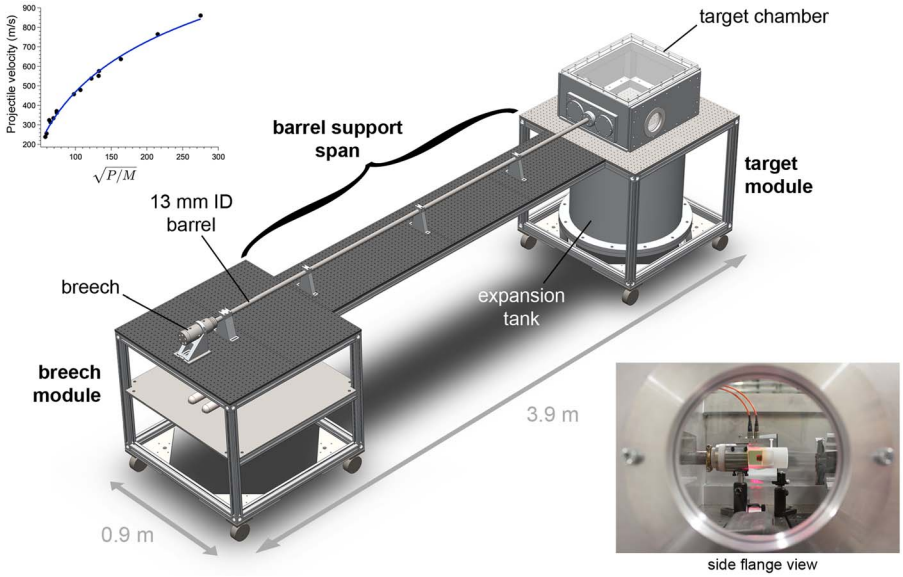

FIG. 3. Model of the portable mesoscale gas-gun designed for the dynamic X-ray imaging experiments, where gas lines and wiring have been removed for clarity. The breech and target tank modules detach from the barrel support span for transport. The gun is capable of launching a 13 mm diameter sabot at velocities nearing 900 m/s, as shown in the upper inset. In these experiments, a concentric interference-fit target alignment system was utilised to reduce experiment turn-around time (lower inset).

selected to provide both a short (~30 ps) X-ray interaction time, and sufficient time following the pulse to integrate the emission from the scintillator.

The requirement at DLS to maintain the storage ring current at approximately 300 mA (and hence individual bunch current for the 2/3 fill of ~0.47 mA) means the potential fill structures are very different to those available at other synchrotrons. For example, the standard fill available at APS, and that used by Luo *et al.*[9–11] consists of 24 singlets, with a bunch current and spacing of 4.25 mA and 153.3 ns, respectively. Luo *et al.*[9–11] employed a combination of fast and slow mechanical shutters to restrict the low energy X-ray (9–13 keV) exposure of the target and diagnostics to 60–100 ms bracketing the dynamic event. They were then able to gate the camera exposure around the sparse 24 singlet structure, selecting the nearest singlet to the time of interest in order to provide time-resolved images.

Due to the low nominal heat load in the hardened X-ray beam it was not necessary to employ mechanical shutters to gate the X-ray exposure of the target and imaging system in the present work. Furthermore, current high-energy shutter technology is not sufficiently developed to enable bunch picking from the hybrid bunch structure on the sub-μs timescale for the large beam sizes employed here. Consequently, it was necessary to gate the image capture system rather than the X-rays, in order to provide time-resolved images. This approach required the use of digital image capture rather than X-ray film as both the target and the downstream imaging system were constantly exposed to the beam. The high-energy X-rays in this work also excluded direct X-ray detection cameras, dictating use of a scintillator coupled imaging system, in which X-rays are absorbed by a scintillator, whose visible output is imaged by an intensified CCD camera as illustrated in Figure 1(a).

The hybrid bunch structure available at DLS provides the opportunity to investigate two modes of X-ray exposure. The first mode involving gating the camera system over the intense singlet in the hybrid structure is similar to that employed previously by Luo *et al.*,[9–11] and was chosen to provide a short (~30 ps) X-ray interaction time. The camera gate (250 ns) was selected to provided sufficient time following the pulse to integrate the emission from the scintillator. The second mode involved gating the camera system over the rising edge of the consecutively filled bunches. In this mode, signal intensity could be increased at the expense of temporal resolution by adjusting the gate width.

C. Mesoscale gas-gun

Dynamic loading was performed using a purpose-built 13-mm bore, single-stage gas-gun, shown schematically in Figure 3. The gun is constructed over a modular extruded aluminium frame, forming a breech module, target module, and barrel support span. The gun extends to 3.9 m in length and 0.9 m in width when fully assembled, and forms a unified optical surface, facilitating precise alignment of the barrel, target, and various diagnostics. The breech and target modules are readily detachable for storage and transport, while the modular nature of the system enables the overall length and specifications of the gun to be adjusted as needed by interchange of the barrel and its support span.

The breech module supports the gas control manifold and gun breech, which is in essence a fast-acting valve that controls the delivery of high-pressure gas from a pair of 0.5 l pressurised charging cylinders filled by the control manifold. Figure 4 provides a schematic of the gas control system and breech operation. The gas-gun is typically operated using high-pressure helium, although nitrogen or argon can be used

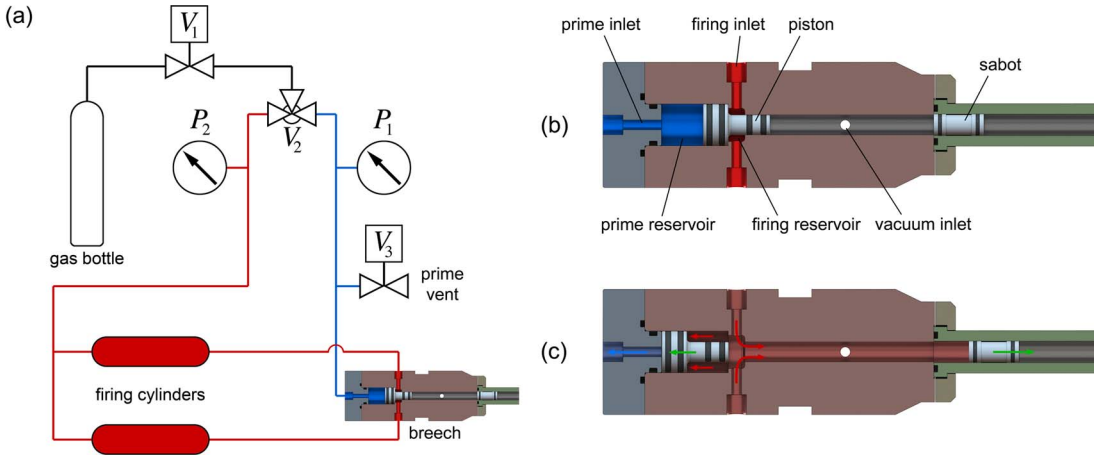

FIG. 4. (a) Schematic of the high-pressure gas delivery system. The prime and firing reservoirs in the breech, highlighted, respectively, in blue and red, are sequentially charged to pressures P_1 and P_2 from a main gas bottle. The firing reservoir is fed directly by two 0.5 l firing cylinders. All valves shown are pneumatically actuated using remote solenoids. (b) Diagram of the reverse-firing breech in its primed state. The piston is held in its forward position by the pressure P_1, and a vacuum is applied to the rear of the sabot. (c) To fire, valve V_3 is opened, which vents the prime pressure P_1, allowing the piston to rapidly move backwards under the action of the firing pressure P_2. Once the firing chamber is cleared, the high pressure gas acts against the sabot, accelerating it down the barrel.

to obtain greater control at lower projectile velocities. The velocity performance for the gas-gun using helium as a driving gas is shown in the inset of Figure 3. The firing process proceeds as follows. A piston is inserted into the breech which seals across the two reservoir ports, separating the firing and priming reservoirs (Figure 4(b)). A priming pressure ($P_1 \geq P_2$) is applied holding the piston in place (coloured blue in Figure 4). The firing cylinders are then charged to the desired firing pressure (P_2) in the range 20–200 bars (coloured red in Figure 4). Firing of the gas-gun is achieved by venting the prime reservoir, causing rapid backwards acceleration of the sealing piston (Figure 4(c)). At the maximum firing pressure, the peak piston velocity approaches 7 m/s when the seal is broken, producing an opening time for the high pressure ports of less than 1 ms, and hence optimal delivery of high pressure gas to the rear of the projectile for good velocity performance.

The target module holds the target chamber and expansion tank. Consisting of a solid, aluminium frame (45 × 60 × 30 cm), and a series of interchangeable side, front, top, and rear flanges, the target chamber provides nearly unrestricted diagnostic access. The aluminium target chamber seals to a half-tapped steel breadboard onto which the diagnostics and target mounting hardware are fastened. The combined volume of the target chamber and expansion tank is approximately 0.3 m^3, ensuring the system remains under vacuum at the highest firing pressures.

Due to the short duration of typical experimental campaigns (3–4 days), a highly repeatable and quick-to-align target mounting system was employed in order to minimise the turn-around time between sequential experiments. This system consisted of a set of concentric sleeves and inserts, which aligned the target impact face to the barrel axis through interference fitting. Aligning of the target proceeded by fully inserting a barrel insert into the end of the cleaned barrel. A target sleeve was fitted over the barrel insert, bringing its clear aperture into position within an outer sleeve alignment ring. Grub screws were then tightened onto the sleeve, fixing its position, and the inner barrel insert withdrawn. The target, mounted on a cylindrical insert, could then be loaded into the sleeve and the impact plane aligned to the X-ray beam using a fixed reference laser diode coaxial with the X-ray beam path. The entire alignment process could be completed within several minutes, while component tolerances constrained target alignment to several mrad.

The gas-gun was installed within EH2, with the target tank mounted on a 1 m diameter 5-axis granite sample stage and the direction of impact perpendicular to the X-ray beam. The impact axis of the gun was raised to 1.4 m, the height of the white X-ray beam in EH2, using aluminium standoff legs at the breech end, and vertical translation of the granite sample stage at the target module end. Rotation alignment was accomplished using the fixed reference laser diode and irises mounted on the target module. Alignment of the impact axis was performed using a spirit level and minute adjustments to the height of the granite sample stage.

An important aspect of the design of the mesoscale gas-gun was its operation through a remote interface, allowing safe control of the complete firing cycle external to the beamline hutch. Operation of the gun was performed through a LabVIEW Graphical User Interface, connected to a remote (10 m cabling) manual control panel through a National Instruments USB DAQ (NI-USB 6009). The GUI controls a sequence of digital relays, which in-turn actuate the various solenoid-driven pneumatic valves and thereby govern the vacuum system and delivery of high pressure helium to and from the prime and firing reservoirs. The position of the various pneumatic valves is actively polled using a Swagelok Valve Control Module (MS-VCMD-6-2) operated over DeviceNet.

D. X-ray and time-resolved diagnostics

As one of the primary objectives is to relate surface-based measurements to physical processes taking place within the bulk of materials, this work explored the simultaneous use of

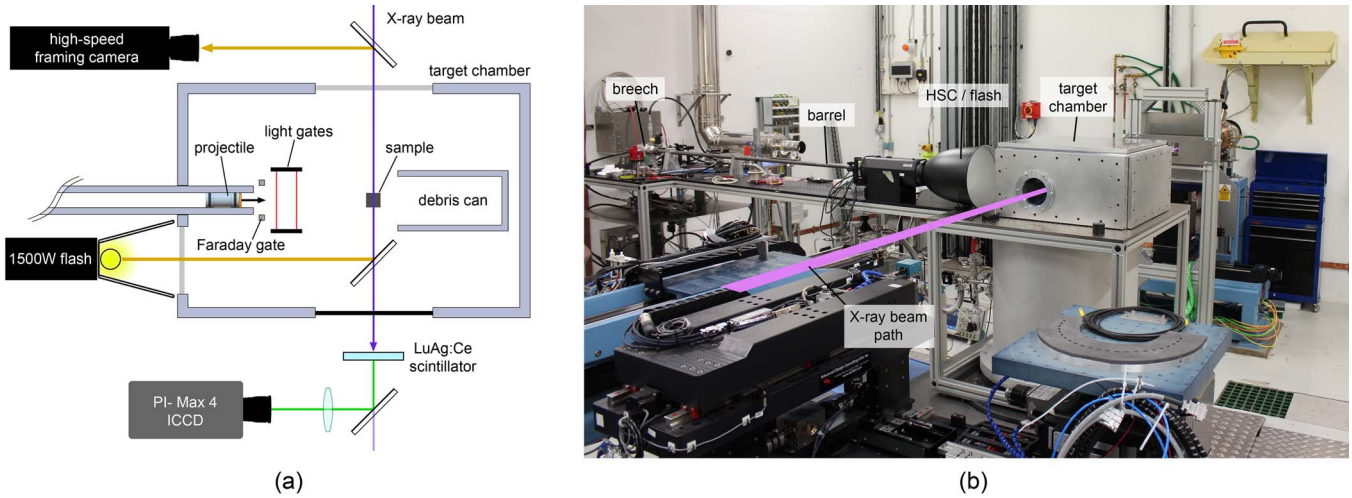

FIG. 5. (a) Detail view of the target chamber, showing the experimental configuration with respect to the various diagnostics and X-ray beam on the I12 beamline at DLS. The windows were made of 5 mm polycarbonate, one of which was tinted black to prevent the flash from interfering with the PI-Max 4 ICCD camera. (b) Photograph of the mesoscale gas-gun setup in EH2. The scintillator and ICCD camera (not shown) were mounted on a large, translation table, which allowed control of the target to scintillator distance.

conventional high-speed imaging and dynamic X-ray imaging. The visible imaging was performed in silhouette using an Invisible Vision Ultra UHSi 12/24 high-speed framing camera (capable of up to 200 $\times$ 10^6 fps), with the flash and high-speed camera removed from the high-energy beam by a pair of turning mirrors inserted within the X-ray beam path. The high speed visible imaging system employed a Nikon 80–200 mm telecentric zoom lens, which yielded a field of view of approximately 95 $\times$ 86 mm, with the objective of providing an overview of the entire experimental process.

The X-ray imaging was performed using a PI-Max 4 intensified CCD camera, with a P46 phosphor and Gen II photocathode, which imaged the visible emission of a scintillator placed in the X-ray beam, downrange from the sample. The scintillator was formed from two LuAG:Ce single crystals, 700 μm thick, placed in series to give a total thickness of 1.4 mm, sufficient to absorb $\sim$74% of the incident X-rays (simulated using XOP[21]) without detrimentally affecting image resolution. The lens employed was a 25 mm focal length Tamron 23FM25SP, used with a 0.5 mm extension ring, giving a magnification of approximately 0.5$\times$. The scintillator was coupled to the lens using a Thorlabs CM1-G01 mounted turning mirror, front surface coated with a protected aluminium reflective layer. In order to maximise the number of photons for this highly transient study, the white beam configuration (4 mm of Cu filter) was used with the X-ray beam apertured to $\sim$13 $\times$ 16.5 mm using the I12 beamline slits, effectively defining the field of view of the X-ray imaging system.

Figure 5(a) presents a top-down view of the target chamber, showing the arrangement of various diagnostics relative to the projectile, sample, and X-ray beam. As shown, the impact axis was oriented normal to the counter-propagating visible and X-ray beams. Also shown are a set of magnetic and optical gates. The magnetic or "Faraday" gate[23] provided an early trigger for the high-intensity flash, allowing it to rise to maximum luminance prior to impact. The projectile velocity was measured using the pair of laser light gates detected using fast photodiodes. A photograph of the gas-gun and associated diagnostics on the I12 beamline is shown in Figure 5(b).

E. Timing and triggering

As briefly discussed earlier, true synchronisation of the gas-gun to the synchrotron, wherein an X-ray bunch arrives at the target at a predefined time after impact, is currently unachievable due to the highly stochastic nature of the firing process, which results in comparatively large uncertainty in the arrival time of the projectile at the sample (on the order of milliseconds for this particular gas-gun). Consequently, a triggering scheme was employed which instead synchronised the image recording system, in this case the PI-Max 4 ICCD camera, with the X-ray bunch closest to the event of interest. In this way, X-ray images could be acquired which maximally exploited the unique structure of the hybrid bunch.

The overall scheme is as follows: A logic scope simultaneously monitored a light gate signal from within the target chamber, and a signal locked to the RF duty cycle of the synchrotron. The logic scope was set to only trigger following a specific sequence of signals, which started with interruption of the light gate signal by the projectile and ended with triggering upon the very next RF signal received. This scheme is depicted in Figure 6(a), which shows the various hardware comprising the triggering system for both the visible and X-ray imaging systems. Also shown in Figure 6(b) is a triggering timeline, where ϕ is the phase offset between the RF signal and X-ray arrival in the experiment hutch, and T the period (orbit time) of the synchrotron. After exiting the barrel, the projectile first passes through the Faraday gate, offset from the target by $\sim$75 mm, which triggers the high-intensity flash used for silhouette imaging with the high-speed framing camera. The projectile next interrupts the two light gates. Interruption of the first light gate triggers a velocity oscilloscope and delay generator, which in turn triggers the high-speed framing camera. The interruption of the second light gate starts the logic scope trigger sequence at **A**, indicated in Figure 6(b).

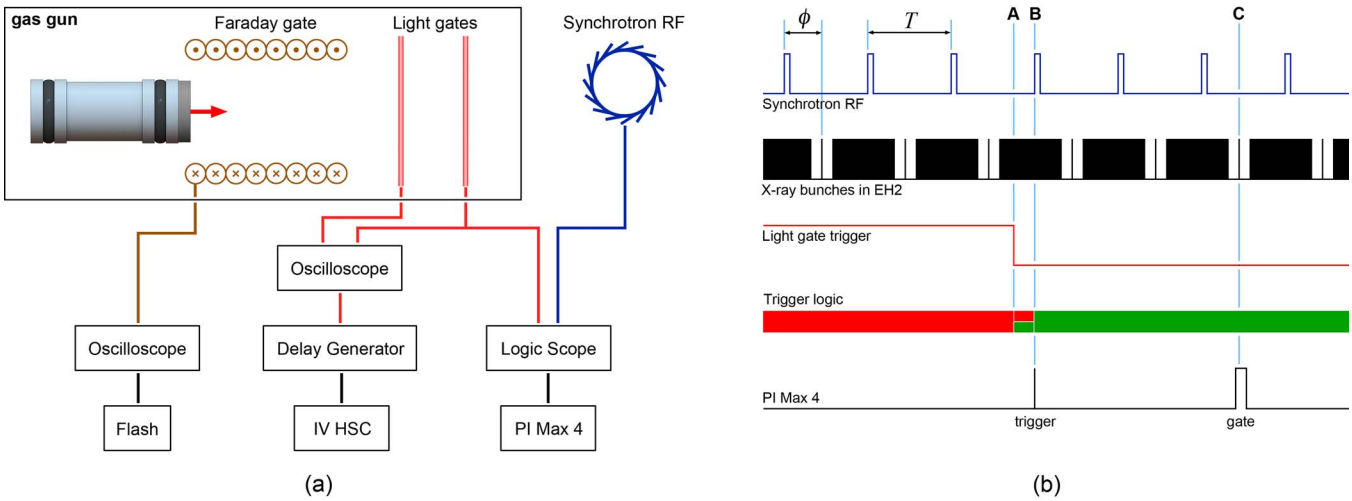

FIG. 6. Triggering scheme for the visible and X-ray imaging cameras. (Left) Upon exiting the barrel, the projectile first passes through a Faraday gate, which triggers a high-intensity flash unit. Breaking of a light gate satisfies one of the triggering conditions of a logic scope. Upon receiving the next RF signal from the synchrotron, the logic scope triggers the PI Max 4 camera. (Right) A signal timeline showing the phase offset ϕ between the RF signal and single X-ray bunch in EH2. The projectile breaks the 2nd light gate at **A**, however the PI Max 4 is not triggered until **B**, upon the subsequent RF pulse. The camera's internal delay is then used to capture the hybrid bunch at **C**.

The very next RF signal is registered at **B**, completing the sequence and ultimately triggering the PI-Max 4 camera. The camera finally acquires an image at **C**, after waiting a predefined delay corresponding to the time of the event of interest and the desired gating mode (single bunch or edge, as shown in Figure 1(b)). The range in temporal offset between the X-ray images and the event of interest, δ, is $-\phi \leq \delta \leq T - \phi$. For the experiments described herein, ϕ was approximately 390 ns, although this depends in particular on the cable lengths and internal response time of the various instruments used.

IV. RESULTS AND DISCUSSION

A series of dynamic X-ray imaging experiments were performed on a range of solid and porous metal targets, impacted at velocities in the vicinity of 400–500 m/s. A majority of the experiments were performed on a selectively laser melted (SLM) steel lattice, which served as an idealised heterogenous material offering regularly spaced microscale features. The lattice was constructed of a periodic array of intersecting rods of diameter 500 μm, forming a repeating cubic unit of 2 mm side length. Samples for this study were electric discharge machined from a larger, 6 mm thick plate into cylinders 10 mm in diameter. A more in-depth characterisation of these SLM lattices, including study of their dynamic behaviour is described by Winter *et al.*[24,25]

A. Scintillator decay response

Prior to each dynamic experiment, an intensity scan through time was performed in order to map the hybrid bunch structure near the desired time interval following impact, ultimately verifying the time delay between the camera trigger and arrival of the 500 ns bunch gap or single bunch in EH2. The PI-Max 4 ICCD camera was configured to capture a sequence of images, of 10 ns gate width, of the unobstructed scintillator (where the beam propagates through the vacuum and windows only) while stepping through a variable gate delay. The top of Figure 7 shows the result of one of these scans, in which each data point represents an average of the frame intensity at a given gate delay time. Comparison with the hybrid X-ray bunch structure (shown along the axis) reveals clear deviation from this ideal behaviour resulting in smearing of the 500 ns gap and single bunch by an extended period of build-up and decay. To better understand the source of this smearing, the scintillator emission was modelled through a convolution analysis using the emission decay response of LuAg:Ce measured by Chewpraditkul *et al.*[26] The calculated result, shown overlaid, reproduces the same features as the measurements, however it indicates a more persistent background resulting in a minimum intensity within the gap of ~0.75 relative to peak. This is a direct consequence of the known long-lived decay behaviour arising from delayed charge carrier recombination in this crystal.[27] Such a long-lived decay will have a marked effect on the effective resolution of gated X-ray images, by contaminating images with a non-negligible background or ghosting.

To assess the actual degree of ghosting in our experiments for the two gating schemes described above, the measured scintillator emission was fitted by adjusting the time constants in a 4 parameter double-exponential representation of the scintillator decay response,

$$I(t) = C_1\, e^{-t/\tau_1} + C_2\, e^{-t/\tau_2}, \qquad (1)$$

where $C_1 = 1.135$, $\tau_1 = 158.9$ ns, $C_2 = 0.139$, and $\tau_2 = 3509.7$ ns. The convolved result, shown at the bottom of Figure 7, fits the entire scintillator build-up and decay cycle more closely. It should be mentioned that these fitted parameters refer to the decay properties of the entire imaging system, including the windows, optical relay elements, and ICCD camera components (photocathode, multi-channel plate, phosphor), and as such should not be considered a measurement of the scintillator response alone. Regardless, the fitted

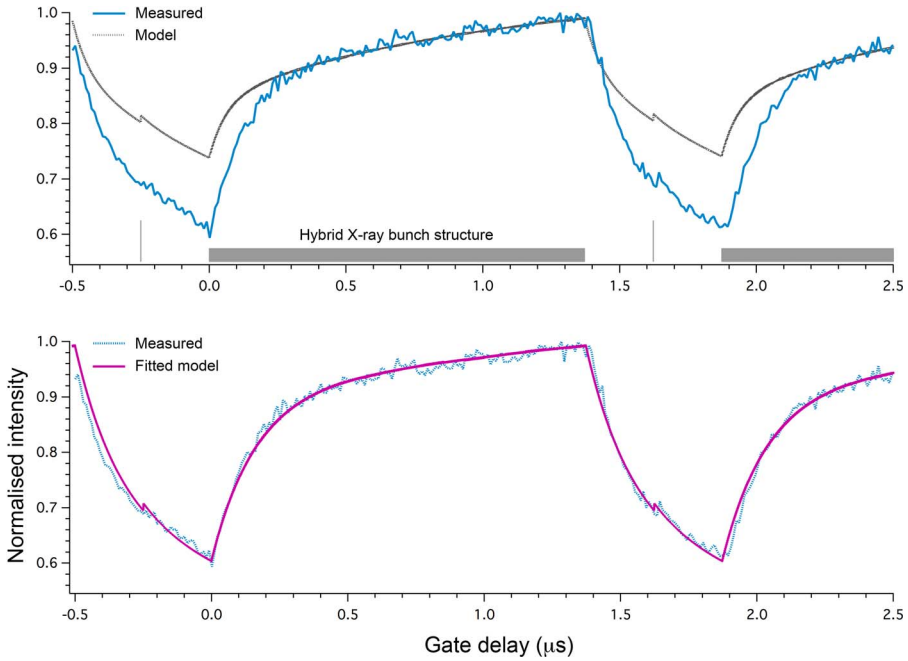

FIG. 7. (Top) Plot showing the measured LuAG scintillator emission obtained from a sweep through gate delay with fixed exposure time of 10 ns. Also shown along the axis is the X-ray bunch structure, which reveals a significant build-up and decay behaviour resulting in pronounced blurring of the 500 ns gap. Despite the 3:1 contrast of the single bunch with respect to the continuous bunches, the long-lived emission of LuAG clearly dominates the signal. An integration model of the scintillator emission based upon measurements by Chewpraditkul *et al.*[26] captures the main features of the emission. (Bottom) A revised model of the scintillator behaviour derived through fitting to experimental data.

model can be used to provide valuable insight into the relative contributions to the overall signal due to ghosting. For the case of gating for 250 ns over the single bunch, ghosting contributes up to 98% of the overall signal. As this background is composed of a nonlinear sum of the information arising from the previous X-ray bunches, correcting for its contribution to image blurring is non-trivial. Gating over the edge for a similar 250 ns reduces this contribution to 84%, although at the obvious expense of time and correspondingly spatial resolution. It should be mentioned that temporal blurring for edge gating is helped by the exponential form of the decay curves, which means that, for the 250 ns example, 90% of the image is formed from light emitted over the first 184 ns.

B. Gating mode comparison

Static X-ray images were taken of the SLM steel lattice to compare the various ICCD gating options presented by the hybrid bunch structure. The image shown in Figure 8(a) resulted from the on-CCD integration of 25 single bunches, where the ICCD gating was set to collect over 250 ns (option 1), as shown in Figure 1(b). Both the lattice and internal free volume are clearly visible, where the decrease in contrast at the upper and lower peripheries is due to the reduced line-of-sight mass from the cylindrical geometry. Figure 8(b) shows an image arising from gating over a lone, single bunch (option 1). Although the signal-to-noise ratio is much reduced, the overall features of the lattice remain discernable. As the scintillator decay measurements revealed however, the majority of the intensity in this image is formed from information originating over the previous several microseconds, which benefits in this case from any lack of sample motion. During a dynamic event regions of the target in motion will superpose, leading to a reduction in contrast and resolution, and hence making this combination of scintillator and gating mode unsuitable for dynamic imaging. The third X-ray image shown

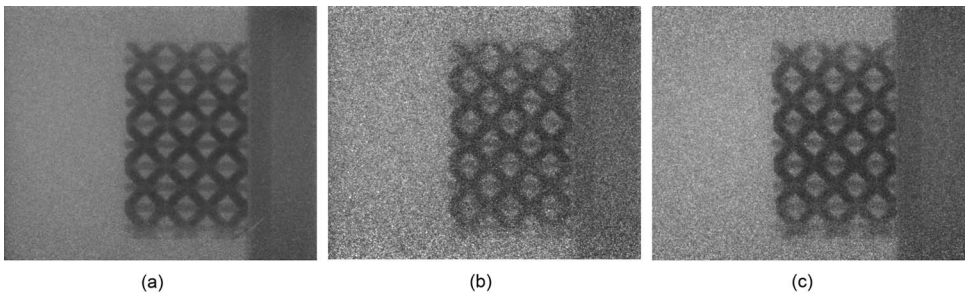

FIG. 8. X-ray images of a SLM stainless steel lattice bonded to a 1 mm thick acrylic plate backed by an acetal sleeve insert, for three different gating schemes: (a) on-CCD accumulation of 25 single X-ray bunches, (b) single bunch gating, and (c) edge gating with a 250 ns gate width. The lattice structure is well resolved in each, with the edge gated image showing a significant improvement in signal-to-noise.

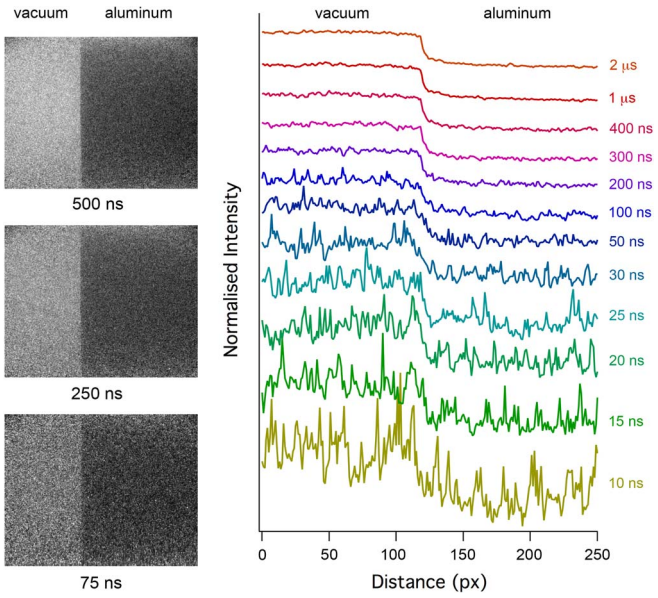

FIG. 9. (Left) Example X-ray images taken in edge gating mode of the free-end of an aluminium rod using three different gate widths. (Right) Averaged line profiles obtained across the free end for gate widths in the range 10 ns−2 μs, showing significant improvement in signal-to-noise above 200 ns. The line profiles are normalised and offset for clarity.

in Figure 8(c) results from gating for 250 ns over the rising edge (option 2) of the 2 ns periodic X-ray bunches. This results in an improved signal-to-noise over the single bunch, and benefits from a reduced contribution from ghosting.

To explore the effect of gate width on signal-to-noise for edge gating, a sequence of images was taken with variable gate width ranging from 10 ns to 2 μs at increments of 5 ns. The ICCD camera viewed the polished free end of a stationary 13 mm diameter Al rod which, as mounted in the target sleeve, closely approximated a knife edge. The results of averaged line-outs taken across the interface are shown in Figure 9(b) for selected gate widths; each trace has been normalised and vertically offset for clarity. As expected, the signal-to-noise ratio improves with longer exposures, where the edge becomes clearly discernable for gate widths above 200 ns. Calculation of the associated edge response function reveals a limiting resolution of ∼6 pixels (154 μm) for the imaging conditions presented here.

C. Dynamic x-ray images

Of the range of impact experiments performed, three are presented here as examples. The first example is the impact of a SLM lattice by an oxygen-free high-conductivity copper flyer at approximately 415 m/s. Figure 10(a) shows the pre-impact condition, again comparing the image quality between an averaged and single-shot (250 ns gate) image. The corresponding dynamic X-ray image, taken 11.4 μs after impact, is shown in Figure 10(b). The lattice is seen to undergo considerable strain with limited penetration into the soft acrylic backer, an attractive design requirement for advanced energy adsorption materials. Details of the local flow in the lattice interstices are obscured, although a possible periodicity can be

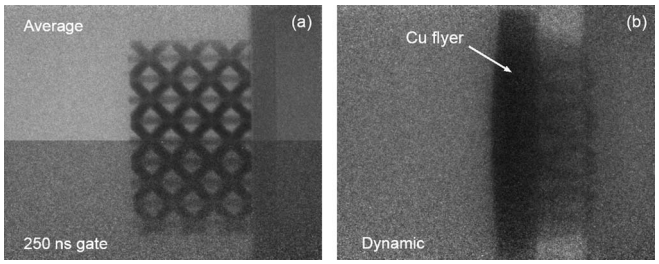

FIG. 10. (a) Static, pre-shot image of an additively manufactured lattice, comparing the signal-to-noise between an averaged image (top) and one obtained using edge gating with a gate width of 250 ns (bottom). (b) A dynamic X-ray image of a copper flyer impacting the SLM steel at 415 m/s, taken 11.4 μs after impact. Possible structure and ordering is still visible in the lattice, although the presence of jets, a future focus of this particular work, will require further development.

seen in the deformed structure. This deformation feature can be used to validate 3D hydrodynamic modelling, as seen in the work by Winter *et al.*,[25] to help further elucidate key deformation modes responsible for energy absorption in these unique class of emergent materials.

The next example, shown in Figure 11, is an experiment performed on an M5 bolt, chosen for its sub-mm periodic thread features. The M5 bolt was impacted by a 3 mm copper flyer at 428 m/s, with simultaneous high speed photography and X-ray imaging. Figure 11(a) shows a sequence of images captured using the high-speed framing camera with an interframe time of 13.3 μs and an exposure time of 1 μs, showing the overall impact process in silhouette. A static X-ray image of the pre-impact condition is shown in Figure 11(b), which draws contrast between the image quality for an averaged image (18 on-CCD accumulations) and one taken with a single, 500 ns acquisition gated within the rising edge. For the latter case, 90% of the resulting image is formed from light emitted over the first 354 ns. Figure 11(c) shows an accompanying dynamic X-ray image taken 12.2 μs after impact, with the same 500 ns edge-gated exposure used previously. The dynamic

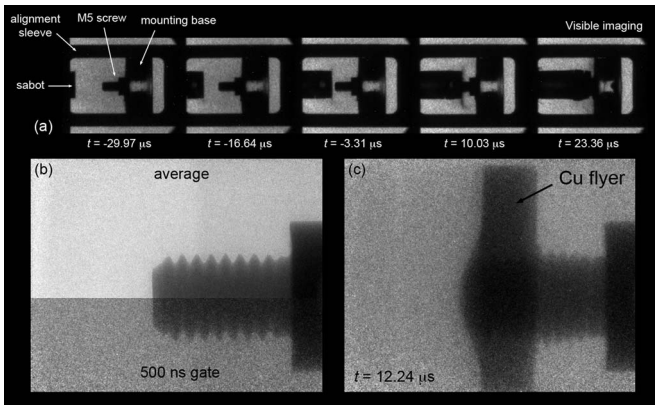

FIG. 11. (a) Static, pre-shot image of an M5 bolt, (top) an average of 18 on-CCD accumulations, (bottom) a single acquisition with 500 ns gate width across the rising edge of the hybrid fill structure. (b) Sequence of silhouette images captured during the impact of a copper flyer onto the M5 bolt, using the high-speed framing camera where time indicates the beginning of the exposure, and $t = 0$ corresponds to impact. (c) A dynamic X-ray image with the same 500 ns gating as in (a), showing slight deformation of the M5 bolt, and clear bulging of the rear of the copper flyer.

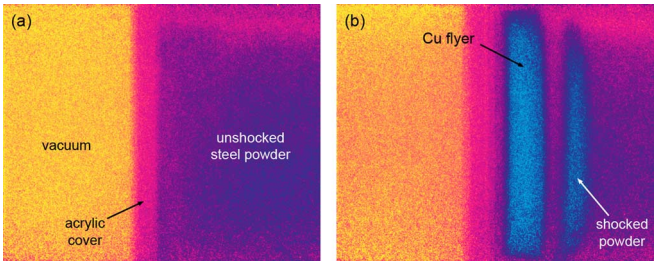

FIG. 12. (a) Static, pre-shot image of a low-density stainless steel powder imaged with a 1500 ns gate width. (b) Dynamic X-ray image capturing the impact of the steel powder by a copper flyer plate at 521 m/s taken 9.5 μs after impact, and the launching of a shock wave. Due to the relatively slow velocities of shocks in powders (few hundred m/s at these impact velocities), the contribution to blurring due to the longer exposure time is less than 1 mm.

X-ray imaging shows clear bulging at the rear of the impactor and penetration of the M5 bolt into the copper. Some of the thread is still discernible within the copper flyer, however the effect of the long scintillator decay makes quantitative estimation of strain challenging. These details however, would normally be obscured in visible imaging, and as such allow additional opportunity for the validation of materials strength models.

The final example is an impact experiment performed on a porous steel powder cell at a velocity of 521 m/s, with the view to demonstrating the ability to image shock waves in flight for a material which undergoes a significant change in density upon impact. Figure 12(a) shows the pre-impact image of the target in false colour, identifying the acrylic cover plate which sealed the steel powder into its cell. Figure 12(b) shows the dynamic X-ray image taken 9.5 μs after impact, where the copper flyer has visibly penetrated the acrylic powder cell. Also clearly visible is an additional high density region ahead of the flyer, corresponding to the shock compressed steel powder. Once again, current visible-based diagnostics are unable to observe the unimpeded progress of the shock wave in opaque materials. This image demonstrates the feasibility of performing in-flight direct measurements of shock velocity and width, and material density behind the shock front.

V. CONCLUSIONS AND FUTURE DIRECTIONS

The investigation of high-rate phenomena using synchrotron facilities promises to bring about a step change in our understanding of dynamic material behaviour. In this paper, we describe a unique capability for studying the physics of dynamic compression in high-Z materials, overcoming the challenges introduced by the requirement for highly penetrating radiation. Our work combines high-energy X-rays with a uniquely flexible bunch structure and new dynamic loading platform to enable subsurface measurements in cm-scale samples of engineering importance. Notably, we demonstrate the rapid installation of a custom, portable mesoscale gas-gun within the confinements of an experimental hutch at the Diamond Light Source. We also showcase the simultaneous use of X-ray imaging and more traditional high-speed framing diagnostics, and describe a method of synchronising the impact and resulting dynamic compression event to the hybrid bunch structure.

One of the challenges identified in this work relates to the performance of the LuAG:Ce scintillator, chosen for its high light output and short initial decay time constant (61 ns).[26] As shown, the LuAG:Ce crystals used in this work also suffer from a long-lived decay component, which results in significant light output over the hybrid bunch gap, effectively dominating the signal around the single bunch. A preliminary survey of alternative scintillator materials suggests a dramatic improvement might be realised by moving to either LYSO or LuI_3, with the contribution due to ghosting dropping to only 2% in the former case.

Additional improvements might also be gained through further sculpting of the 2/3 fill structure. Although gating over the rising edge provided the best compromise between signal and background in this work, a significant portion of the emission is contained within the decay tail. Moving to a burst of sequential bunches within the gap (e.g., 8–12 singlets) would provide a direct means of both increasing signal intensity and permitting integration of the decay while maintaining a short effective exposure time (16–24 ns in this example). This could be extended further by prescribing a new fill mode comprised of multiple, uniformly spaced bursts, which would have the additional benefit of reducing the apparent period of the fill mode, leading to reduced jitter between X-ray imaging timing and the dynamic event of interest, which in the current work was limited to one revolution of the electron storage ring.

The final obvious area for development involves improving the efficiency of the imaging system downstream from the scintillator. The use of a faster lens system and advanced intensifier technology would greatly enhance light yield, improving signal-to-noise and hence permitting shorter effective exposure times.

ACKNOWLEDGMENTS

The work described in this paper would not have been possible without the assistance of numerous persons, for which the authors are very grateful; Michael Drakopoulous, Thomas Connolley, and Bob Humphreys from the I12 beamline for their support during the beam time; Norman Randall for assistance with transport and setup of the equipment; Mark Collinson, Simon Finnegan, David Jones, Sam Stafford, and John Winters for their help with the experiments; John McCaffrey and Manjul Shah from Princeton Instruments for helpful advice and loan of the PI-Max camera; Stephen Johnson and David Pitman for preparation of the samples. The authors would also like to extend their gratitude to Michael Rutherford for many fruitful discussions following the experimental campaign. This work resulted from time awarded by Diamond Light Source under proposal EE8863.

The Institute of Shock Physics acknowledges the continued support of AWE and Imperial College London.

[1] A. S. Balchan, J. Appl. Phys. **34**, 241 (1963).
[2] P. A. Rigg, C. L. Schwartz, R. S. Hixson, G. E. Hogan, K. K. Kwiatkowski, F. G. Mariam, M. Marr-Lyon, F. E. Merrill, C. L. Morris, P. Rightly, A. Saunders, and D. Tupa, Phys. Rev. B **77**, 220101 (2008).

[3]V. Yuan, J. Bowman, D. Funk, G. Morgan, R. Rabie, C. Ragan, J. Quintana, and H. Stacy, Phys. Rev. Lett. **94**, 125504 (2005).
[4]F. E. Merrill, D. Bower, R. Buckles, D. D. Clark, C. R. Danly, O. B. Drury, J. M. Dzenitis, V. E. Fatherley, D. N. Fittinghoff, R. Gallegos, G. P. Grim, N. Guler, E. N. Loomis, S. Lutz, R. M. Malone, D. D. Martinson, D. Mares, D. J. Morley, G. L. Morgan, J. A. Oertel, I. L. Tregillis, P. L. Volegov, P. B. Weiss, C. H. Wilde, and D. C. Wilson, Rev. Sci. Instrum. **83**, 10D317 (2012).
[5]S. Le Pape, L. Divol, L. Berzak Hopkins, A. Mackinnon, N. B. Meezan, D. Casey, J. Frenje, H. Herrmann, J. McNaney, T. Ma, K. Widmann, A. Pak, G. Grimm, J. Knauer, R. Petrasso, A. Zylstra, H. Rinderknecht, M. Rosenberg, M. Gatu-Johnson, and J. D. Kilkenny, Phys. Rev. Lett. **112**, 225002 (2014).
[6]M. Koenig, A. Ravasio, A. Benuzzi-Mounaix, B. Loupias, N. Ozaki, M. Borghesi, C. Cecchetti, D. Batani, R. Dezulian, S. Lepape, P. Patel, H. S. Park, D. Hicks, A. Mckinnon, T. Boehly, A. Schiavi, E. Henry, M. Notley, R. Clark, and S. Bandyopadhyay, Astrophys. Space Sci. **307**, 257 (2007).
[7]L. M. Hull, G. T. Gray III, and B. J. Warthen, J. Appl. Phys. **116**, 043504 (2014).
[8]R. L. Sandberg, C. Bolme, K. Ramos, Q. McCulloch, J. L. Barber, R. Martinez, M. Greenfield, S. D. McGrane, B. Abbey, A. Schropp, F. Sieboth, P. Heiman, B. Nagler, E. C. Galtier, and E. Granados, CLEO: 2014 Postdeadline Paper Digest, paper STh5C.8, 2014.
[9]B. J. Jensen, S. N. Luo, D. E. Hooks, K. Fezzaa, K. J. Ramos, J. D. Yeager, K. Kwiatkowski, T. Shimada, and D. M. Dattelbaum, AIP Adv. **2**, 012170 (2012).
[10]S. N. Luo, B. J. Jensen, D. E. Hooks, K. Fezzaa, K. J. Ramos, J. D. Yeager, K. Kwiatkowski, and T. Shimada, Rev. Sci. Instrum. **83**, 073903 (2012).
[11]B. J. Jensen, C. T. Owens, K. J. Ramos, J. D. Yeager, R. A. Saavedra, A. J. Iverson, S. N. Luo, K. Fezzaa, and D. E. Hooks, Rev. Sci. Instrum. **84**, 013904 (2013).
[12]E. Seppälä, J. Belak, and R. Rudd, Phys. Rev. Lett. **93**, 245503 (2004).
[13]C. Reina, J. Marian, and M. Ortiz, Phys. Rev. B **84**, 104117 (2011).
[14]J. P. Escobedo, E. K. Cerreta, D. Dennis-Koller, B. M. Patterson, and C. A. Bronkhorst, J. Phys.: Conf. Ser. **500**, 112023 (2014).
[15]B. Wang, J. Li, J. Sun, X. Luo, Z. Liu, and H. Liu, J. Mater. Eng. Performance **23**, 1896 (2014).
[16]Y. Yang and B. F. Wang, Mater. Lett. **60**, 2198 (2006).
[17]W. W. Chen, M. C. Hudspeth, B. Claus, N. D. Parab, J. T. Black, K. Fezzaa, and S. N. Luo, Philos. Trans. R. Soc. A **372**, 20130191 (2014).
[18]G. W. Laabs, D. J. Funk, and B. W. Asay, Rev. Sci. Instrum. **67**, 195 (1996).
[19]A. D. LeGrand, W. Schildkamp, and B. Blank, Nucl. Instrum. Methods Phys. Res. A **275**, 442 (1989).
[20]H. Moini, C.-L. Kuo, and J. C. Bilello, Nucl. Instrum. Methods Phys. Res. A **280**, 137 (1989).
[21]R. J. Dejus and M. Sanchez del Rio, Rev. Sci. Instrum. **67**, 3356 (1996).
[22]R. P. Walker, in *Proceedings of the APAC*, Indore, India, 2007, http://www.jacow.org, pp. 66–70.
[23]M. Yokoo, N. Kawai, Y. Hironaka, K. G. Nakamura, and K.-I. Kondo, Rev. Sci. Instrum. **78**, 043904 (2007).
[24]R. E. Winter, M. Cotton, E. J. Harris, D. J. Chapman, and D. E. Eakins, J. Phys.: Conf. Ser. **500**, 142034 (2014).
[25]R. E. Winter, M. Cotton, E. J. Harris, J. R. Maw, D. J. Chapman, D. E. Eakins, and G. McShane, Modell. Simul. Mater. Sci. Eng. **22**, 025021 (2014).
[26]W. Chewpraditkul, L. Swiderski, M. Moszynski, T. Szczesniak, A. Syntfeld-Kazuch, C. Wanarak, and P. Limsuwan, IEEE Trans. Nucl. Sci. **56**, 3800 (2009).
[27]M. Nikl, Phys. Stat. Sol. A **202**, 201 (2005).